MoS<inf>2</inf> supported on P25 titania: A model system for the activation of a HDS catalyst

MoS_2 supported on P25 titania: a model system for the activation of a HDS catalyst

M. Signorile, A. Damin, A. Budnyk, C. Lamberti, A. Puig-Molina, P. Beato, S. Bordiga

J. Catal., **328** (2015) 225-235

DOI: 10.1016/j.jcat.2015.01.012

http://www.sciencedirect.com/science/article/pii/S0021951715000226

MoS_2 supported on P25 titania: a model system for the activation of a HDS catalyst[§]

M. Signorile,[a] A. Damin,[a] A. Budnyk,[a,c] C. Lamberti,[b,c,*] A. Puig-Molina,[d] P. Beato,[d,*] S. Bordiga,[a]

[a] Department of Chemistry, NIS Interdepartmental Center, INSTM Reference center, University of Turin Via Quarello 15 A, I-10135, Torino, Italy.
[b] Department of Chemistry and CrisDi Interdepartmental Center, University of Turin Via P. Giuria 7, I-10125 Torino, Italy.
[c] Southern Federal University, Zorge street 5, 344090 Rostov-on-Don, Russia.
[d] Haldor Topsøe A/S, Nymøllevej 55, 2800 Kgs. Lyngby, Denmark.

Corresponding authors: Carlo Lamberti carlo.lamberti@unito.it and Pablo Beato pabb@topsoe.dk

Abstract
In this work we investigate two activation procedures for a MoS_2/TiO_2 model catalyst. When the activation is performed in two-steps, by sequentially dosing first H_2S followed by reduction in H_2, an intermediate Mo-oxysulfide phase forms, leading finally to a 3-4 layers thick nano-MoS_2 phase. Conversely, when the activation is performed in a single-step by dosing H_2S and H_2 simultaneously, the activation proceeds via a layer-by-layer growth, leading to a MoS_2 structure remarkably different from conventional MoS_2. To achieve this structural understanding, a well-defined model system was synthesized and a multitechnique approach has been applied to characterize the growth and surface properties of MoS_2 on TiO_2. The results evidence the complexity of the structural evolution during the activation procedure and the sensitivity of the final product to subtle changes in the activation procedure. Catalytic tests determined that the one-step activation of MoS_2 on TiO_2 results in a more active HDS, HDN and HYD catalyst, as expected due to smaller MoS_2 nanoparticles in terms of both average diameter of the plates and number of stacking layers.

Keywords
MoS_2; TiO_2; X-RAY-ABSORPTION-SPECTROSCOPY; RAMAN; HYDRODESULFURIZATION CATALYSTS; HYDROTREATING CATALYSTS; CARBON-MONOXIDE; CO ADSORPTION; IN-SITU

[§]In honor to Haldor Topsøe, a pioneer and visionary who has shaped the field of heterogeneous catalysis for almost a century. He has been a driving force in the development of advanced *in-situ* characterization techniques and thereby influenced to a great extent the authors' field of activity. PB would like to express his deepest gratefulness to Haldor Topsøe for giving him the possibility to follow his passion and being a source of inspiration also beyond science.

1. Introduction

Molybdenum disulfide (MoS_2) is an inorganic layered compound belonging to the family of metal dichalcogenides [1, 2]. MoS_2 is characterized by a well-known layered structure leading to a

series of unique features. The physical-chemical properties of MoS_2 are size-dependent, particularly for nanometric crystals they are closely related to the morphology, i.e. the extension and number of layers of the nano-crystals. MoS_2 has been successfully applied in several fields, such as opto-electronics [3, 4], tribology [5], photocatalysis [6, 7] and in heterogeneous catalysis in particular as a hydrotreating catalyst in oil refining [8-10].

Hydrotreating is an important step in oil-refinement, because it leads to a removal of heteroatoms like S, N, O and metals, which are naturally present in crude oil. The cleaned, hydrotreated feedstock can then be processed further in other refining processes, where the catalyst would otherwise suffer severe deactivation due to the poisoning effect of the heteroatoms [11]. Moreover, effective hydrotreating of the various feedstocks in a refinery is absolutely necessary to meet the environmental legislations, which are progressively lowering the allowed amount of heteroatom impurities in transportation fuels [12, 13].

An industrial hydrotreating catalyst is actually a complex material, where MoS_2 is grown *in situ* on a high surface area support (typically alumina and or silica-alumina) in presence of promoters such as Co or Ni. The final composition can contain more than 20 wt% of Mo and up to 10 wt% of Co/Ni.

The catalytic properties of MoS_2 seem to be closely related to the particle shape and dimension of the nano-crystals so that a careful control of the material preparation is mandatory to obtain the desired properties [8, 14-16]. For research purposes, top-down or bottom-up approaches can be followed to obtain highly dispersed MoS_2 nano-particles. In the case of a top-down approach, bulk particles of MoS_2 can be exfoliated (as in the case of graphene) in order to study the effects of the degree of layer stacking. This exfoliation can be performed in several ways (exfoliation [17, 18], sonication in a solvent till to obtain a suspension [19] or intercalation [20]). Conversely, following a bottom-up approach, MoS_2 can be grown *in situ* in a sulfiding atmosphere from a Mo-oxide precursor (typically prepared via impregnation of a Mo salt) [21, 22] or by direct decomposition of a Mo-S containing precursor [23]. As sulfiding reagent, typically H_2S in H_2 is used, but also CS_2 [22] and organosulfides [24] have been successfully applied to convert the precursor into MoS_2. The nature of the support, in terms of chemical composition and surface properties, plays a fundamental role during the growth of the sulfide phase [22, 25-27]. As the process is proposed to occur at sulfur coordination vacancies placed on the edges of MoS_2 particles [8, 28], usually a small particle size combined with a good dispersion is expected to lead to the exposure of a large number of active sites. The combination of all the above mentioned parameters will finally determine the catalyst performance.

Great part of our current fundamental understanding of hydrotreating catalysts has been achieved via molecular modelling [29-31] or experimentally, involving extremely simplified systems [32, 33]. A possible way to move forward is to try to reproduce the key features of a real catalyst on a proper designed "*model system*". In this work, we have chosen to use an unpromoted (Mo-only) catalyst, with low metal content, supported on titania (Degussa P25). The relatively narrow particle size distribution and good crystallinity of the titania is very useful in limiting the heterogeneity of the supported species providing the possibility of establishing a clear relationship between spectroscopic fingerprints and reactivity of the catalyst.

To obtain a structural understanding at the molecular level, we have followed the formation of the supported MoS_2/TiO_2 along two parallel activation methods: a single-step method (or direct method), where a mixture of H_2S and H_2 is dosed simultaneously and a two-step method (or indirect method), where H_2S is dosed first and H_2 is dosed in a successive step. A combination of X-Ray diffraction (XRD), IR spectroscopy of adsorbed CO, UV-Vis, Raman, X-Rays adsorption (XANES and EXAFS) spectroscopy techniques provided a unique set of data and new insight into the structural and electronic properties of MoS_2 based hydrotreating catalysts. Furthermore the post activation morphology of the catalysts has been evaluated through transmission electron microscopy (TEM).

Once invited to contribute to the prestigious special issue that J. Catal. dedicated to Haldor Topsøe, we decided to submit our joint work on MoS_2/TiO_2 because Haldor has personally contributed (or has strongly encouraged) for decades the research on hydrodesulfurization catalysts.

More than hundred papers have been published by scientists form Haldor Topsøe A/S on this topic, among all: [10, 21, 29, 32-47].

2. Experimental

2.1. Sample preparation

An unpromoted MoS_2 catalyst (3 wt.% Mo loading) supported on TiO_2 has been prepared by incipient wet impregnation of the P25 (Degussa: 60 m^2g^{-1} from producer) with an aqueous solution of AHM ($(NH_4)_6Mo_7O_{24}\bullet 4H_2O$; produced by Merck, Art. 1182). The impregnated sample has been dried in air at room temperature over night and then finely grinded.

2.2. Sample activation

Two different sulfidation procedures (activation methods) were applied in order to obtain highly dispersed MoS_2:

Two-steps activation method: The sample is activated in dynamic vacuum at 773 K for 1h and then oxidized in pure oxygen at the same temperature (50 mbar equilibrium pressure inside the cell). The oxidized sample is sulfided in pure H_2S at 573 K for 2.5h (50 mbar equilibrium pressure inside the cell) and afterwards reduced for 3h in H_2 at the same temperature (100 mbar equilibrium pressure inside the cell). This sample has been successively further sulfided at 673 K, following the same methodology. After the high temperature sulfidation, the reduction stage has been performed first at 573 K and then at 673 K. All steps have been followed by *in situ* characterizations (i.e. avoiding the re-exposure of the sample to air after each treatment).

Single-step activation method: After 2h of calcination in static air, the sample is introduced either into a reactor (a modified Linkam CCR1000 [48] for Raman measurement (Figure S1), or on a house-made reactor cell [49] for XAFS. In both cases, the sulfidation has been conducted in a flow of 5% H_2S in H_2 (25 ml/min), with a temperature ramp of 5 K/min up to the target sulfidation temperature and held there for 30 minutes. In order to avoid temperature effect during spectra acquisition, the sample was quickly cooled to room temperature in inert flow (He) before each measurement. For the Raman experiments, a further check on data reliability is provided by the addition to the sample of a 10 wt% of Si powder: the frequency of the characteristic Raman band of silicon (520 cm^{-1} at RT) is in fact red-shifted as the temperature is increased. In case of Raman spectra we have followed five different steps (473 K, 523 K, 573 K, 623 K and 698 K) while, in the case of XAFS measurements only 2 steps (573 K and 698 K) were considered. A schematic drawing of the temperature profiles of this activation method is reported in Figure S2 of the supplementary contents.

2.3. Sample characterization

According to the applied treatment, different characterization techniques have been used. *In situ* Fourier transform infrared (FTIR) spectroscopy of CO adsorbed at 77 K, Raman, diffuse-reflectance UV-Vis spectroscopy and X-Ray Powder Diffraction (XRPD) have been applied for the sample activated with the two-steps method. *In situ* Raman, and X-ray absorption fine structure (XAFS, both in its X-ray absorption near edge structure, XANES, and extended X-ray absorption fine structure, EXAFS, regions) spectroscopies have been used to characterize the sample treated activated with the single step method. *Ex situ* HRTEM has been performed on the samples after the last sulfidation for both treatment procedures.

2.3.1. Two-steps activation method

X-Ray Powder Diffraction patterns have been collected with a PW3050/60 X'Pert PRO MPD diffractometer from Panalytical working in Bragg–Brentano geometry, using as source the high power ceramic tube PW3373/10 LFF with a Cu anode (λ=1.541 Å), equipped with a Ni filter to attenuate the k_β line. A RTMS (Real Time Multiple Strip) and X'celerator as detector. Samples have been measured in 0.8 mm diameter capillary, sealed under N_2 controlled atmosphere. Patterns were collected in the $10° \leq 2\theta \leq 90°$ range (corresponding to 1.09 Å < *d* < 8.84 Å *d*-spacing interval), with a 0.02° step in 2θ.

Raman measurements have been performed on a Renishaw inVia Raman Microscope spectrometer, working in backscattering mode equipped with an Ar^+ laser emitting at 514.5 nm. The effects of radiation damage on the sample were systematically studied by collecting successive series of spectra at different laser powers, concluding that working with 1% of the maximum laser power (i.e. less than 1 mW on the sample) was a safe experimental condition. All reported spectra were collected reducing the power of the laser down to this value. The measurements have been carried out in controlled atmosphere in a house-made optical quartz cuvette cell, focussing the laser on sample trough a 20x long working distance objective.

UV-Vis-NIR spectra have been collected on a Varian DRUV Cary 5000 spectrometer, equipped with a diffuse reflectance sphere. Measurements have been performed directly on powders, using a sample holder specific for diffuse reflectance. The sample holder has been filled and sealed inside a glove box avoiding air exposure. Because of the strong optical absorption of the samples (related both to the TiO_2 ligand to metal charge transfer and to the MoS_2 transitions) a post treatment dilution in a low absorbing material has been performed in order to obtain reliable signals. In particular the samples have been mixed with polytetrafluoroethylene powder (Aldrich) in a 1:15 weight ratio in the case of oxidized sample; while in the case of sulfided samples, the black nature of MoS_2 required a 1:50 dilution.

Infrared analysis has been performed on a Bruker Vertex 70 FTIR, equipped with a HgCdTe cryogenic detector. Spectra were collected at a resolution of 2 cm^{-1}, averaging 32 scans. The sample has been prepared as thin pellet and measured in an in-house-made cryogenic cell. In order to perform the measurements at 77 K, liquid nitrogen has been used as cooling bath. The spectra have been collected on the sample in contact with CO equilibrium pressures (P_{CO}) in the 0 – 40 mbar range at 77 K.

HRTEM images have been collected with a JEOL 3010-UHR operating at 300 kV, equipped with a 2 k × 2 k pixels Gatan US1000 CCD camera. The samples (previously suspended in ethanol) have been deposited on a copper grid covered with a lacey carbon film. The average thickness and diameter of the MoS_2 have been evaluated considering approximately 140 different particles.

2.3.2. Single-step activation method

Raman measurements have been performed on a Horiba Jobin Yvon LabRam HR confocal microscope, focussing sample through a 10x long range objective. Also in this case the 514.5 nm Ar^+ line has been used as excitation source. However, a different strategy has been followed in order to carry out the measurements keeping the highest possible laser power at the sample. The modified Linkam CCR1000 reactor cell [48] exploits the sample fluidization, so that the exposure time to the

laser beam of each particle of the sample is reduced, preventing the radiation damage even at high laser power (see Figure S1 of the supplementary content). In order to achieve the best fluidization conditions, a sieve fraction of the sample particles with size comprised between 150 μm and 300 μm has been selected. Moreover, as maxima position of the bands depend on the temperature at which the Raman spectra are collected [50, 51], each spectrum has been collected at room temperature. The experimental procedure adopted for the sulfidation followed by *in situ* Raman is reported in Figure S2 of the supplementary content, that illustrates the temperature profile (heating rate set to 5 K/min; a 25 ml/min flow rate used for both He and 5:95 H_2S:H_2 sulfiding mixture).

XAFS experiments were performed at ANKA-XAS beam line [52] in Angströmquelle Karlsruhe Synchrotron Facility (Karlsruhe, Germany). The Mo K-edge data was collected in transmission mode using the Si(111) double crystal monochromator and a vertical opening of 0.45 mm to enhance the energy resolution. A beam size of 8x0.45mm was used to overcome the possible inhomogeneity of the sample. Three ionization chambers were used to detect the intensity of the incident and transmitted X-rays. A Mo metal foil was located between the second and third ionization chambers to calibrate the energy of the XAFS spectra. The data was collected *in situ* using a reactor cell [49]. A sieved fraction of sample in the 75 – 125 μm range was introduced in the reactor.
The extraction of the $\chi(k)$ function was performed using the Athena program [53]. The k^2-weighted $\chi(k)$ functions have been Fourier transformed in the 2.0 – 16.0 $Å^{-1}$ k-range. Phases and amplitudes of the different scattering paths have been calculated using FEFF-6 code [54] and have been checked on a spectrum of bulk MoS_2. The fit of the EXAFS bulk MoS_2 was performed on an extended Δk range of 2.0 - 16.0 $Å^{-1}$, adopting as input the structure obtained from a XRD reference (PDF no. 037–1492, with $r_{Mo\text{-}S}$ = 2.366 Å and $r_{Mo\text{-}Mo}$ = 3.161 Å), investigating the R-space in the ΔR = 1.0 – 7.5 Å range ($2\Delta k\Delta r/\pi > 57$). All the 109 possible single and multiple scattering paths, having a relative amplitude higher than 10% (with respect to the first shell path amplitude), have been considered in the fit. In order to reduce the number of independent variable in the fit, a single S_0^2 amplitude factor and a single energy shift parameter ΔE have been adopted for all paths. Moreover the path distance and the corresponding Debye-Waller factor have been optimized in an independent way only for the first two (more intense) single scattering paths, which are the first Mo–S and the second Mo–Mo shells. All remaining 107 paths have been optimized using only two additional fitting parameters that are: (i) an isotropic expansion parameter α able to describe each path length as $r_i = r_i^0 (1+\alpha)$ (being r_i^0 the path length expected from the XRD model, i = 3, ... 109); (ii) a single Debye-Waller factor (σ^2) that allows to rescale the Debye-Waller factors of all paths on the basis of the corresponding path length according to the following approximate model: $\sigma_i^2 = \sigma^2 (r_i^0/r_1^0)^{1/2}$ (being i = 3, ... 109 and being r_1^0 = 2.366 Å) [47, 55, 56]. The quality of the fit, that was excellent, can be appreciated in Figure S7 of the supplementary content, while the numerical values of the eight optimized parameters are summarized in the last column of Table 2.
The overall S_0^2 and the first and second shell Debye-Waller factors $\sigma^2_{Mo\text{-}S}$ and $\sigma^2_{Mo\text{-}Mo}$ values derived for the fit of the bulk MoS_2 reference have successively been transferred to all fits on the supported MoS_2 samples as fixed parameters.
Owing to the lower S/N ratio of the EXAFS data collected on the MoS_2 supported samples, the k^2-weighted $\chi(k)$ functions have been Fourier transformed in the shorter 2.0 – 13.5 $Å^{-1}$ k-range and the corresponding fits were performed in R-space in the reduced ΔR = 1.0 – 3.2 Å range ($2\Delta k\Delta r/\pi > 16$). Only two single scattering paths (one for Mo-S and the other for Mo-Mo, accounting for the 1st and the 2nd coordination sphere) were included in the fit. The geometrical model adopted is the same of the bulk MoS_2 but restricted to the second coordination shell.

HRTEM images were acquired using a Phillips CM200 electron microscope at 200 kV. The TEM samples were prepared by dispersing them in ethanol and drop-casting onto a Cu grid with holey

carbon support. The average thickness an diameter of the MoS_2 have been evaluated considering approximately 300 different particles.

2.4. Catalytic tests

For the catalytic tests both samples were first calcined at 500 °C in static air. For the different activation procedures the samples were prepared as a sieve fraction (600-850 μm) and transferred to a tube furnace, connected to a gas dosing station. For the one-step activation method the sample was heated with 5 °C/min in 10% H_2S/H_2 to 425 °C and kept at that temperature for one hour, while for the two-steps activation the sample was first sulfided with 5 °C/min in 10% H_2S/He to 400 °C for one hour and then reduced at the same temperature in a flow of pure H_2 for another hour. After activation, the samples were taken out of the tube furnace and transferred directly (with short contact to air) to the test reactor. The catalytic testing was performed in a fixed bed reactor charged with 300 mg catalyst in the fraction 600-850 μm. To achieve a steady flow the catalyst was mixed with Ballotini glass balls (150-250 μm) until a final volume of 1 ml was obtained. To pressurize the system, prior to catalytic test the one-step activated sample was treated in a flow of 2.5 % dimethyldisulfide (DMDS) dissolved in *n*-heptane at 350 ºC and 50 bar. Helium was used as a carrier gas with a flow of 250 Nml/min. Instead, for the two-step activated sample a flow of 250 Nml/min pure H_2 was used to achieve the equal pressure and temperature. After 4 hours of stabilization, the feed was changed to a model oil feed containing 3 % dibenzothiophene (DBT), 0.5 % indole (IND), 1 % naphthalene (NAP), 2.5 % dimethyldisulfide (DMDS), 0.5 % *n*-nonane, the rest being *n*-heptan solvent. This feed allows to verify the activity in hydrodesulfurization (HDS), hydrodenitrogenation (HDN) and hydrogenation (HYD) reactions. The catalytic reaction was also performed at 350 ºC, 50 bar using helium as a carrier gas with a flow of 250 Nml/min. The employed feed rate of oil was 0.5 ml/min and the total weight hourly space velocity (WHSV) was 68 h^{-1}. The products from the reaction were analysed by an on-line GC equipped with a FID using *n*-nonane as an internal standard. The reaction was allowed to stabilize over 4 hours in order to obtain steady state conditions after changing to the oil feed prior to catalytic measurements. Afterwards eight GC analyses of the product stream were made with 1 hour intervals.

3. Results and discussion

3.1. Two-steps activated MoS_2/TiO_2: bulk characteristics by XRPD, Raman and UV-Vis-NIR

XRPD, Raman and UV-Vis-NIR spectroscopy have been combined to study the evolution of the bulk structural and electronic properties of the sample before and after the activation steps.

Figure 1 reports the XRPD data of the freshly impregnated sample after calcination in pure O_2 at 773 K (curve **A**) and after sulfidation at 573 and 673 K in H_2S (curve **B** and **C,** respectively). For comparison, the XRPD patterns of the pure TiO_2 support are included at the bottom of Figure 1. While calcination in O_2 and sulfidation at 573 K does not provoke the formation of an additional long-range ordered phase, a new crystalline phase is observed for the sample sulfided at 673 K (curve **C**). The two new diffraction peaks at 2θ values of 31.16° (d = 2.869 Å) and 58.98° (d = 1.565 Å), are assigned to {100} and {110} planes of MoS_2 (PDF no. 037–1492). The absence of the main reflection from the {002} planes of bulk MoS_2 (expected at 2θ between 14° and 15°) indicates a small crystalline domain size of the MoS_2 particles along the c axis. The peculiar pattern of the sample sulfided at 673 K, showing {100} and {110} planes of MoS_2 and the absence of the reflection from the {002} planes suggests a preferential growth of the MoS_2 particles along the "in-plane" direction, while the stacking of layers along the c axis seems to be limited. It is worth noting that together with the appearance of the crystalline domains of MoS_2 an increase of the diffuse scattering between ~ 15–30° 2θ is observed as well, indicating the progressive increase of an amorphous phase upon sulfidation.

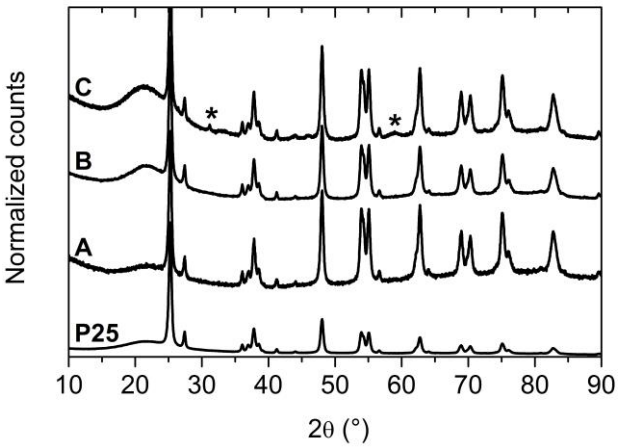

Figure 1. XRPD patterns, collected using λ = 1.541 Å, of, from bottom to top: bare **P25**; MoO_x/TiO_2 after oxidation performed at 773 K in pure O_2 **A**; Mo-S/TiO_2 species formed after sulfidation in static atmosphere performed at 573 K **B**; and, as **B**, but sulfidating at 673 K **C**. The ***** labels the reflections ascribable to MoS_2. All patterns are normalized to the main anatase reflection (2θ = 25.29°) intensity and vertically shifted for sake of clarity.

Raman spectroscopy can give further insight on the structural evolution of the Mo phase, as the presence of extended crystalline domains is not required to obtain an informative spectrum. Figure 2 shows the spectra obtained for the O_2-calcined sample (curve **A**) and after its sulfidation in H_2S at 573 and 673 K (curve **B** and **C,** respectively). The spectrum of the calcined material is dominated by the vibrational fingerprint of anatase (peaks at 143 cm^{-1}, 395 cm^{-1}, 516 cm^{-1} and 640 cm^{-1}) while bands related to the rutile phase are not observed [46, 57]. The intense and broad band centred at 980 cm^{-1} suggests the presence of a high amount of terminal Mo=O sites [58]. This can be explained by assuming the presence of very small particles or clusters, with a high surface to bulk ratio. The position and broad character of the band is quite different from the characteristic bands of the Mo-precursor (AHM, see Figure S3 of the supplementary content) and indicates a (partial) decomposition of the precursor during the thermal treatment. The presence of a weak but sharp band at 820 cm^{-1} reveals the formation of a small fraction of crystalline α-MoO_3. The second most intense band of α-MoO_3 at 996 cm^{-1} falls into the broad band at around 980 cm^{-1} and is therefore not discernible. The small amount and/or small crystallite size of α-MoO_3 is in agreement with the XRPD measurements, which did not shown any signal ascribable to crystalline α-MoO_3.

After the treatment in H_2S at 573 K the broad Mo=O related band is strongly decreased in intensity, indicating the structural transformation of the MoO_x species. At this stage the doublet of A_{1g} and E^1_{2g} bands, which univocally characterize the Raman spectrum of MoS_2, is not clearly observed. Anyhow, a new quite intense and sharp band has emerged at 445 cm^{-1} and the anatase peak at 395 cm^{-1} is partially overlapped with a very broad band extending between 250 and 400 cm^{-1}. The appearance of a band at ~440 cm^{-1} during the transformation of an oxidic Mo-phase into a sulfided Mo-phase has been observed earlier [18, 59, 60], and has been ascribed to the formation of an intermediate Mo-oxysulfide phase.

Only after the sulfidation at 673 K the signals of MoS_2 are clearly visible in the Raman spectrum, which shows a doublet of sharp peaks with maxima at 407 cm^{-1} and 383 cm^{-1}, ascribable to A_{1g} and E^1_{2g} vibrational modes respectively [18, 22, 61, 62]. The A_{1g} mode defines a vibration along the stacking of MoS_2, while E^1_{2g} is a mode characteristic of the lateral extension of the MoS_2 sheets. Both signals are quite asymmetric, suggesting the presence of a variety of MoS_2 species characterized by slightly different nuclearity. The contribution of the sites located on particles boundaries can be considered as well, suggesting a small dimensionality of the sulfide particles. In a number of recent reports, a relationship between the position of the A_{1g} and E^1_{2g} vibrational modes and the number of layers in the MoS_2 particles has been elaborated [18, 61, 62]. Most of these studies consider materials which have been obtained by the top–down method, via exfoliation of bulk MoS_2, i.e. deposited on a flat (single crystalline) support. However, the relationship has not been systematically investigated

for MoS_2 particles grown on oxide particles as support (bottom-up method). In the latter case the shape and positions of the MoS_2 Raman bands might be directly affected by the morphology (i.e. effect of particle roughness and curvature) and surface properties of the support (i.e. preferential growth on specific crystal faces and surface defects). Applying the established relationships to our MoS_2/TiO_2 system, results in an average stacking of 3-4 layers per particle could be estimated. This is not in complete agreement with XRPD, since MoS_2 particles composed of 3-4 layers should provoke a (002) reflection. This observation reinforces our reasonable suspicion that the A_{1g} and E^1_{2g} peak positions cannot be taken as direct reference of MoS_2 staking in the case of highly dispersed supported MoS_2.

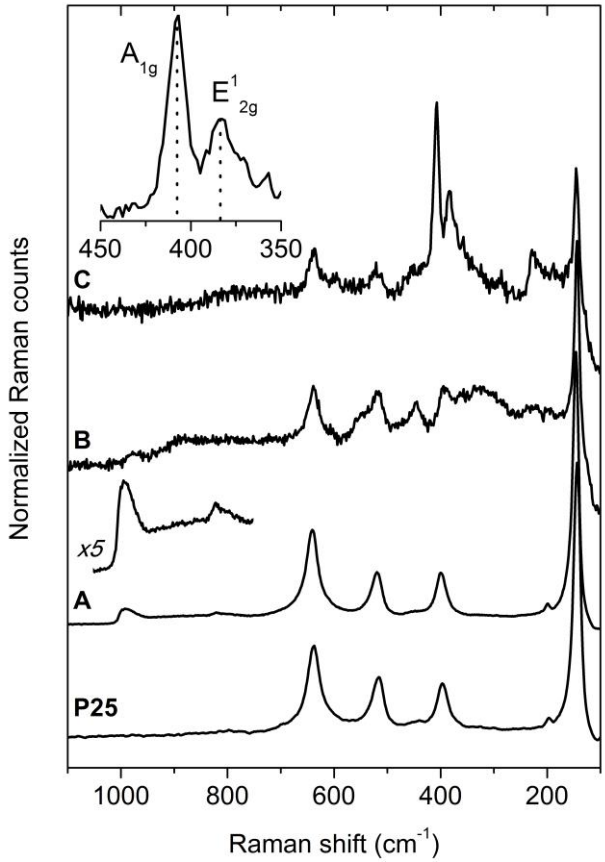

Figure 2. Raman spectra (λ = 514.5 nm) of, from bottom to top: bare **P25**; MoO_x/TiO_2 after oxidation performed at 773 K in pure O_2 **A**; Mo-S/TiO_2 species formed after sulfidation in static atmosphere performed at 573 K **B**; and, as **B**, but sulfidating at 673 K **C**. The inset shows a detail of the A_{1g} and E^1_{2g} doublet of MoS_2 for the sample after the sulfidation performed at 673 K. All the spectra are normalized on the main anatase peak (143 cm^{-1}) intensity and vertically shifted for sake of clarity.

Because of the close relation between optical properties of MoS_2 and its morphology, a characterization through diffuse reflectance spectroscopy (DRS), in the UV-Vis-NIR region, can give further structural information on the growth of the sulfided phase as well as on its electronic structure. The DRS-UV-Vis-NIR spectra of the same samples after oxidation and sulfidation at two temperatures are given in Figure 3, together with spectrum of the bare titania (P25) as reference.
Upon comparison of the DRS-UV-Vis-NIR spectra of the bare titania with the oxidized sample (**P25** and **A** curve of Figure 3), a red shift of the absorption edge of titania is observed. The pale yellow colour of the MoO_x/TiO_2 sample can be explained by considering the effect of the presence of a MoO_x phase due to the impregnated species. No other signals ascribable to any *d-d* transitions associated to the Mo centres, suggest that Mo species have a d_0 electronic configuration (i.e. Mo, lies in the 6+

oxidation state), while in presence of Mo^{5+} and/or Mo^{4+} sites different *d-d* transitions falling in the visible region are expected [22, 63, 64].
The effect of sulfidation at 573 and 673 K on the optical properties of the sample is reported in Figure 3, curves **B** and **C** respectively. Even for the low temperature sulfidation (573 K), the sample turns very dark to almost black in color, showing a continuous absorption over the entire Visible-NIR region. This behaviour is consistent with a reduction of Mo^{6+} to $Mo^{[6-x]+}$ (with x=1-2), and changes in the coordination sphere. After the sulfidation at 673 K, the optical spectrum of the sample shows the typical features of MoS_2: two new signals are observed in the range 18000-14000 cm^{-1} assigned to the A_1 and B_1 excitonic transitions at the K point of Brillouin zone [22, 65]. With respect to the data reported for a bulk MoS_2 [22], both the transitions are blue shifted suggesting a quantum confinement of the excitons, due to the low dimensionality of the MoS_2 particles [66], which is in agreement with the results obtained from the XRPD. This quantum effect has been described hypothesizing a low dimensionality of the MoS_2 particles along the *c* direction (i.e. these are characterized by a low number of layers). However the quantum confinement can be in principle due to a small size of the MoS_2 along the "in-plane" *a* and *b* directions as well, as the particles can be characterized by a confinement along both the directions simultaneously.

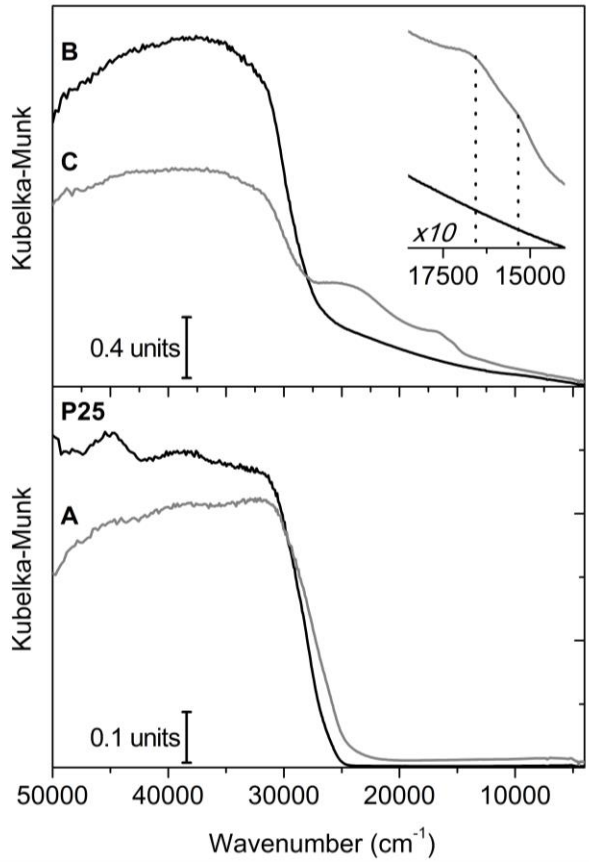

Figure 3. DRS-UV-Vis-NIR spectra of, from bottom to top: bare **P25**; MoO_x/TiO_2 after oxidation performed at 773 K in pure O_2 **A**; Mo-S/TiO_2 species formed after sulfidation in static atmosphere performed at 573 K **B**; and, as **B**, but sulfidating at 673 K **C**. The inset shows a detail of the MoS_2 excitons region for the sulfided samples.

3.2. Two-steps activated MoS_2/TiO_2: surface characterisation by in situ CO adsorption at low temperature followed by FTIR spectroscopy.

FTIR spectroscopy of CO adsorbed at low temperature is a powerful technique providing detailed information on the surface properties of a material, because of its sensitivity to the coordination environment and to the oxidation state of the exposed sites [67-69]. Figure 4 reports, in the CO

stretching region, the background subtracted spectra obtained upon dosing 40 mbar of CO at 77 K on the samples (bold black curve) and progressive outgassing (thin grey curves), down to a residual CO equilibrium pressure (P_{CO}) below 10^{-3} mbar (bold grey curve). The spectra have been collected in the same cell where the sulfidation and H_2-reduction processes have been performed. This procedure allows us to probe the surface of the activated catalyst directly after the sequence of *in situ* treatments, without exposing the sample to ambient environment. The evolution of the FTIR spectra upon decreasing P_{CO} allows us to discriminate among sites with different adsorption energies [67-69]. Panels **(a)-(f)** of Figure 4 have been collected on the same pellet. This approach makes quantitatively significant the change of intensities of the different bands along the six successive treatments that are described in the following.

The set of spectra reported in panel **(a)** of Figure 4, corresponding to the calcined MoO_x/TiO_2 sample, is dominated by the intense band at 2138 cm^{-1}, assigned to "liquid-like" CO physisorbed on the surface [70, 71]. The other main features in the spectra can be assigned to CO probing the different Ti sites exposed on activated TiO_2. According to the detailed assignments reported by Mino et al. [72] the main bands are assigned as follows. The band at 2168 cm^{-1} is related to CO adsorbed on Ti^{4+} sites on flat (001) faces, while the band at 2185 cm^{-1} is due to CO adsorbed on Ti^{4+} sites on (101) and (112) faces. This last band is very broad and it possibly contains also a component at 2179 cm^{-1}, which is assigned to CO adsorbed on Ti^{4+} sites on (100) faces. All bands assigned to $Ti^{4+}\cdots CO$ complexes undergoes the expected frequency shift upon decreasing P_{CO} due to the modulated lateral-lateral interactions between adjacent CO oscillators at changing CO coverages on the surface of TiO_2 [43, 45, 67-69].

The only vibrational feature which can be related to the presence of Mo sites is the weak band at 2200 cm^{-1}, possibly related to the presence of defective Mo^{5+} sites [73]. The low intensity of this feature suggests that the MoO_x phase is characterized by metal sites with a high coordination, making the CO adsorption possible only on defects and edge sites. This hypothesis is supported by the fact that the 2200 cm^{-1} band does not shift in frequency with the CO coverage, indicating that we are dealing with isolated Mo^{5+} sites, as expected for defect sites.

In panel **(b)** of Figure 4, the formation of new surface sites can be recognized by the spectral changes observed after sulfidation in H_2S at 573 K. The appearance of signals at frequencies below that of "liquid-like" CO, evidences the formation of surface sites characterized by π-back donation character [69, 74]. In particular, a broad band, with a maximum centered at 2116 cm^{-1}, can be related to the presence of sites with a reduced character, possibly Mo^{4+} sites of a newly formed MoO_xS_y phase [22]. The high intensity of this signal implies a relative high abundance of coordinatively unsaturated metal sites accessible to CO. Upon reducing the P_{CO}, the slight difference in the desorption rates (due to a different adsorption strengths) and the loss of the "liquid-like" CO signal, evidences that the band at 2116 cm^{-1}, actually consists of at least two components, shifted to relatively higher and lower frequency side of the center at 2116 cm^{-1}. Even at the lowest P_{CO}, a complete desorption of the CO from the two Mo sites is not observed, indicating a strong adsorption energy at these sites. Considering the components separately, no shifts occur along the desorption of CO, suggesting the isolate nature of such sites. The most intense component in panel **(a)**, i.e. the signal of CO adsorbed on (001) anatase faces at 2168 cm^{-1}, is strongly reduced; this suggests that the newly formed MoO_xS_y phase preferentially grows on this surface.

The most relevant effects of subsequent sulfidation at 673 K, panel **(c)**, is the restoration of the band centred at 2168 cm^{-1}, the decreased intensity of the band at 2116 cm^{-1} and the appearance of a new band at 2067 cm^{-1} (broad and asymmetric toward lower frequencies). The latter can be ascribed to reduced Mo sites characterized by a different environment, and possibly higher electron density, related to the loss of oxygen (electron withdrawing). By lowering the P_{CO}, it is possible to observe again the strong blue shift of the two bands at 2168 and 2183 cm^{-1}, confirming their assignment to terrace surfaces, exposing a high density of Ti^{4+} sites, each able to adsorb a CO molecule at high coverages.

The effect of hydrogen on the nature of Mo-S sites, has been investigated as a function of the sulfidation and successive reduction temperatures. In particular the sample sulfided at 573 K was treated in H_2 at the same temperature (panel **(d)**) while, the sample sulfided at 673 K, was reduced at 573 K (panel **(e)**) and at 673 K (panel **(f)**). The most relevant effect of H_2 reduction at 573 K on the sample sulfidated at the lower temperature, is the intensity enhancement of the band at 2116 cm^{-1}, testifying the capability of hydrogen to react with the sulfur atoms (Mo-S sites) exposed on the external surfaces of the particles: these sulfur atoms are eliminated as H_2S molecules and more coordinatively unsaturated Mo sites become accessible to CO.

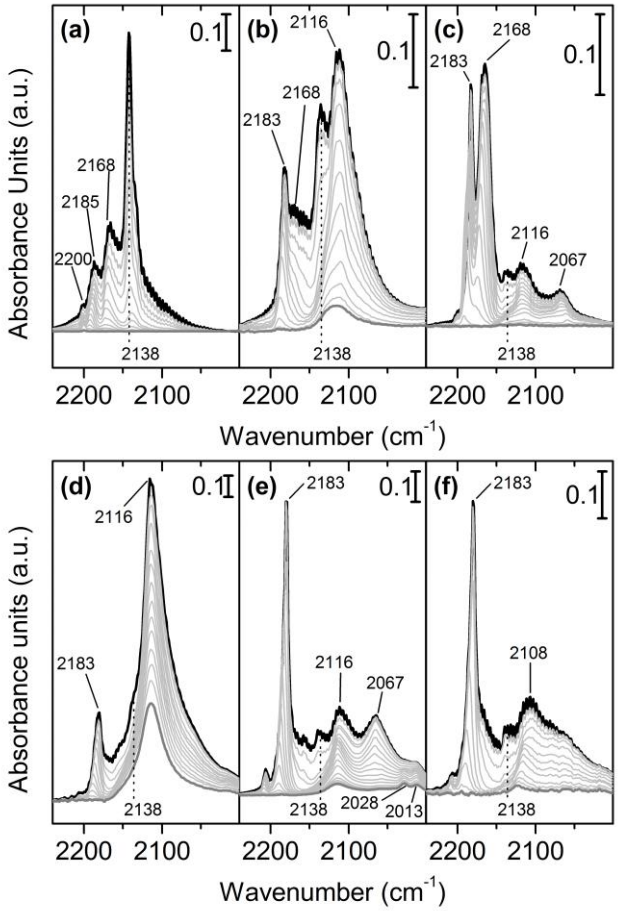

Figure 4. Background subtracted FTIR spectra of CO adsorbed at 77 K on: MoO_x/TiO_2 sample treated in oxygen at 773 K **(a)**; Mo-S/TiO_2 sample after sulfidation in static atmosphere performed at 573 K **(b)**; at 673 K **(c)**; effect of successive reduction in H_2 at 573 K of the sample sulfided at 573 K **(d)**; effect of successive reduction in H_2 at 573 K of the sample sulfided at 673 K **(e)**; effect of successive reduction in H_2 at 673 K of the sample sulfided at 673 K **(f)**. Black lines show the spectra collected at maximum CO coverage (i.e. 20 mbar equilibrium pressure) while gray lines describes the evolution of the system upon the progressive CO desorption. Bold grey lines correspond to the spectra collected after 30 min of outgassing.

The effects of H_2 treatment on the sample sulfided at 673 K are different depending on the reduction temperatures. With respect to panel (**c**), upon reducing the sample at 573 K, the overall intensity of the signals related to Mo is increased. From a qualitative point of view, the reduction produces a substantial increase and differentiation of the population of Mo sites which become accessible to CO (panel **(e)**). Indeed, at the highest P_{CO}, a broad absorption is extending on the right hand of the 2067 cm^{-1} band down to 1990 cm^{-1}, from which two bands are clearly emerging at 2028 and 2013 cm^{-1}, upon lowering P_{CO}. Contrarily to the component at 2067 cm^{-1}, these new features are not fully removed upon decreasing P_{CO} below 10^{-3} mbar, reflecting a stronger adsorption energy. Also the band centered at 2116 cm^{-1} shows a residual of adsorbed CO. This fact suggests that the nature of the sites related to this signal after the reduction treatment is different in comparison with the adduct resulting in a similar C-O stretching frequency in the only-sulfided sample in panels **(b)** and **(c)**. This

assignment is in agreement with the different P_{CO}-dependent frequency shift undergone by the component around 2116 cm^{-1} in panel **(e)** and in panels **(b)**, **(c)**. However the assignment of these signals to precise adsorption sites is impossible without the support of molecular modelling. After a further increase of the reduction temperature up to 673 K, panel **(f)**, an even larger variety of Mo sites become available to be explored by CO, resulting in a continuous absorption from 2108 cm^{-1} and extending below 2000 cm^{-1}. Independently to the sulfidation and to the reduction temperatures, the band at 2168 cm^{-1} is no longer observed after interaction with H_2, see panels **(d)-(f)**. Combining all these observation, it is possible to hypothesize that upon thermal treatment at 673 K particles grow with partial uncovering (001) anatase faces. Moreover, the formation of larger MoS_2 particles is associated with a decrease of the number of very defective boundary sites (represented by 2116 cm^{-1} band) and the increase of the less unsaturated sites, that can be associated to the band at 2068 cm^{-1} as reported in literature for analogous studies of unsupported MoS_2 [75]).

3.3. *Single-step activated MoS_2/TiO_2: Raman and XAFS.*

The Raman spectrum collected after calcination in static air is comparable to that obtained in case of the sample oxidized in oxygen in static condition (see Figure S3 of the supplementary information). Both spectra are characterized by a broad band with a maximum at 985 cm^{-1}, associated to the presence of MoO_x/TiO_2 phase. The series of spectra recorded during sulfidation are reported in Figure 5. After thermal treatment in H_2S/H_2 flow at 473 and 523 K a broad asymmetric band at ~400 cm^{-1} starts to grow. In the same spectral region, the band due to TiO_2 at 395 cm^{-1} is located, but the broadness of the observed band and its evolution with temperature allows us to assign the band to a vibration associated to a growing Mo-sulfide phase. For the Raman spectrum collected after sulfidation at 573 K the appearance of the A_{1g}, E^1_{2g} doublet characteristic of MoS_2 can be clearly recognized. The position of both bands significantly deviates from the values reported in the literature for bulk and even single layer MoS_2. Both, A_{1g} and E^1_{2g} peaks are very low in frequency compared with previously reported data. In fact the position of the first band suggests a MoS_2 monolayer, while the second maximum is compatible with the band position ascribed for a bulk system. The reliability of the data is confirmed by the position of the silicon band used to monitor the sample temperature which doesn't show any significant shift among all the measurements (Figure S6). Moving to the higher temperature steps (623 and 698 K), the Raman signals increase in intensity and, simultaneously, their width is reduced. This fact can be related to an increase of the particles sizes. The higher intensity can be due to the increase of the scattering centres (i.e. of more extended MoS_2 domains), while the sharpening of the peaks can be explained by a more homogenous distribution of particles sizes and morphologies. Along temperature increase treatment, the slight but continuous red shift of the E^1_{2g} mode and the increase of the separation $\Delta\nu$ between the doublet (see Table 1), can be qualitatively interpreted by considering an increased stacking. It is important to note, in Figure 5, the absence of a band at ~440 cm^{-1} at intermediate temperatures, indicating that the structural transformation from MoO_x phase to MoS_2 during direct activation follows a different pathway compared to the two step activation (see Figure 2), i.e. not involving the formation of Mo-oxysulfide species.

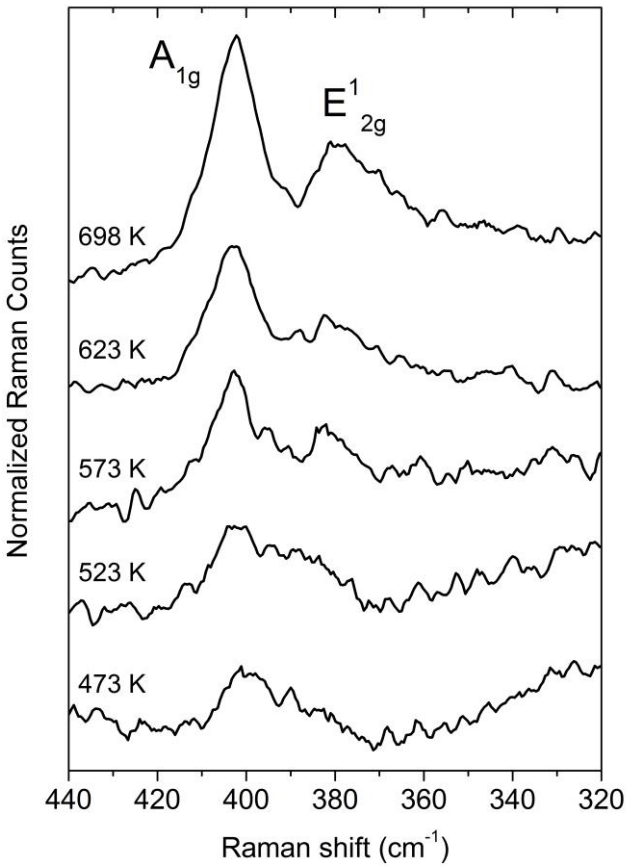

Figure 5: Raman spectra collected on MoS_2/TiO_2 sample during sulfidation in H_2S/H_2 mixture for five rising temperatures.

Table 1: Estimated positions of A_{1g} and E^1_{2g} Raman bands, and corresponding separation Δv, of MoS_2 for each sulfidation temperature of single-step activation method.

Temperature (K)	A_{1g} (cm^{-1})	E^1_{2g} (cm^{-1})	Δv (cm^{-1})
473	399.9	\\	\\
523	401.5	\\	\\
573	402.1	383.4	18.7
623	402.1	382.2	19.9
698	402.1	381.3	20.8

Because of its atomic selectivity [44, 76], XAFS is one of the most suitable technique to follow the evolution of the Mo coordination sphere in nanostructured supported phases [77].
Considering the starting material (calcined in air, curve **A**), the simultaneous presence of different MoO_x structures is very probable: comparing the XANES part of the spectrum with the reference α-MoO_3 it is possible to observe that the MoO_x/TiO_2 phase lies in the same oxidation state (i.e. +6) of the bulk oxide. The Mo in the two materials probably has a similar coordination environment too, as testified by the presence of the same pre edge feature in both the spectra. The EXAFS spectrum of MoO_x/TiO_2 phase instead shows a very broad peak in the first coordination shell (between 1-2 Å, related to Mo-O and Mo=O bonds), quite different from the well-defined signal of bulk α-MoO_3. This complexity reflects also the heterogeneity of the Mo-O bonds assuring the grafting to the TiO_2 surface. Moreover the signal of the second coordination shell is almost negligible for sample **A**, while

the α-MoO_3 shows a clear Mo-Mo contribution between 3-4 Å. The structure of the MoO_x/TiO_2 phase is definitely different from a bare α-MoO_3, making a fit of the data very complex, time consuming and beyond the scope of the present work.
Moving to the sulfidation of sample performed at 573 K (curve **B**), both XANES and EXAFS regions of the spectrum show a deep transformation of the system: the XANES is characterized by a red shift of the absorption edge which underlines the reduction of Mo^{6+} to Mo^{4+}. Quantitatively, the edge position almost coincides with the one of the reference bulk MoS_2 (Table 2). The |FT| of EXAFS function is characterized by the appearance of two new peaks, testifying a complete modification of the first and the second coordination shells of Mo. Comparing these features with those of the MoS_2 bulk phase, it is possible to observe that they fall at the same distances, comparing the corresponding imaginary parts it is evident that the two signals have the same phase on the supported materials and in MoS_2 bulk. Consequently, EXAFS spectroscopy has proved that, locally, the MoS_2 particles show a geometry identical to the one of the bulk material. Conversely the intensities of these signals substantially differs from the ones of the bulk material, with a second peak much less intense compared with the one of the reference. The MoS_2 particles are not fully coordinated in the second shell, testifying their low dimensionality. This qualitative observation is quantitatively confirmed by the results of the EXAFS fits reported in Table 2.

The XANES of the sample sulfided at 698 K (curve **C**) perfectly overlaps the one of the sample sulfided at the lower temperature, while the EXAFS shows an increased intensity of the peak related to the second coordination shell. According to the fit performed, the coordination number of the second shell rises to $N_{Mo} = 2.1$ after this treatment. This value is still lower than the one expected for a bulk MoS_2 ($N_{Mo} = 6.0$), but the trend gives an idea about the particles growth of the MoS_2 nanoparticles. In particular, the increased coordination number in the second shell suggests that the lateral growth of the MoS_2 particles is favoured at higher sulfidation temperatures. This datum is in agreement with the result of Raman which shows a similar trend.

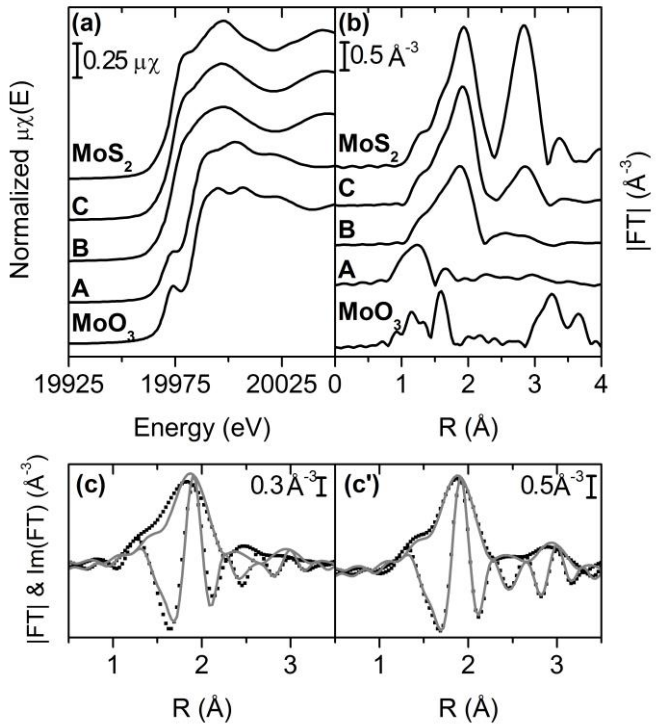

Figure 6: XANES spectra **(a)** and |FT| of EXAFS **(b)** spectra of, from bottom to top: bulk **MoO_3**, Mo-oxides/P25 after air calcinations at 773 K **A**; Mo-S/P25 species formed after sulfidation performed in gaseous flow at 573 K **B**; as **B**, but sulfidating at 698 K **C**; and bulk **MoS_2**. The imaginary parts and the magnitudes of FT (dots) and the relative fits (solid gray lines) for the sample sulfided at 573 K and for the sample sulfided at 698 K are reported in parts **(c)** and **(c')**, respectively, together with the corresponding best fit (black lines).

Table 2. Summary of the fits on the EXAFS spectra of the sample sulfided at 573 K **B** and 698 K **C** with the single-step activation method compared with values of a reference bulk **MoS_2**. The absence of error bars implies that the corresponding parameter has been fixed in the fit. The XRD reference (PDF no. 037–1492, with $r_{Mo\text{-}S}$ = 2.366 Å and $r_{Mo\text{-}Mo}$ = 3.161 Å) has been used as geometrical input for the fits. The higher shells paths and the multiple scattering paths of bulk MoS_2 have been optimized according to the isotropic expansion approximation [47, 55, 56] using as unique parameters α and σ^2 , that have been optimized as follows: α = + 0.006 ± 0.001 and σ^2 = 0.0042 ± 0.0006 Å^2.

	B	**C**	**MoS_2**
Edge position (eV)	19973.8	19973.8	19973.2
Δk (Å^{-1})	2.0 – 12.0	2.0 – 12.0	2.0 – 16.0
Δr (Å)	1.0 – 3.2	1.0 – 3.2	1.0 – 7.5
S_0^2	0.86	0.86	0.86 ± 0.06
ΔE (eV)	1.0 ± 2.0	1.2 ± 0.8	1.4 ± 0.6
N_S	3.3 ± 0.3	4.8 ± 0.2	6.0
N_{Mo}	1.0 ± 0.4	2.1 ± 0.3	6.0
$r_{Mo\text{-}S}$ (Å)	2.39 ± 0.01	2.402 ± 0.005	2.401 ± 0.004
$r_{Mo\text{-}Mo}$ (Å)	3.16 ± 0.03	3.169 ± 0.009	3.166 ± 0.003
$\sigma^2_{Mo\text{-}S}$ (Å^2)	0.0026	0.0026	0.0026 ± 0.0005
$\sigma^2_{Mo\text{-}Mo}$ (Å^2)	0.0025	0.0025	0.0025 ± 0.0003

3.4. *Ex situ* HRTEM

HRTEM micrographs have been collected ex situ after the last sulfidation step for both activation treatments. Some representative images are shown in Figure 7 (a-d): for both activation procedures the sulfidation leads to the formation of well-defined sulfide particles. The measured distance between crystal planes is 0.6 nm, which matches the {002} interplanar spacing of MoS_2 obtained from diffraction data (PDF no. 037–1492), and confirms the formation of molybdenum disulfide phase. Slight differences between the two samples are revealed by the statistical analysis of the images (Fig.7 e, f): for the two-steps activation, the MoS_2 phase is characterized by well separated particles, with an average stacking of 2-3 layers per particle and an average length perpendicular to the stacking direction comprised between 2 and 6 nm. The single-step activated sample conversely shows a larger abundance of MoS_2 particles close to each others, in average of smaller size compared to the two-steps activated sample (average stacking of 1-2 layers, average particles length in the 2-4 nm range). Furthermore, the MoS_2 particles grown by the two-steps method appear to have a more well-defined planar morphology, while for the single-step activation the particles generally have a more bent morphology, indicating the presence of a considerable number of defects.
The comparison of the morphologies of the two differently activated samples shows how the growth of the MoS_2 phase is strongly affected by the reaction environment. A possible explanation can be given considering the role of hydrogen during sulfidation: the H_2 might inhibit the formation of extended MoS_2 domains due to its capability of removing sulfur atoms from the coordination environment of molybdenum, leading to smaller and defect-rich particles. Instead, when the sulfidation mixture contains only H_2S, the MoS_2 layers can grow more regular, leading to larger and well-crystallized particles.

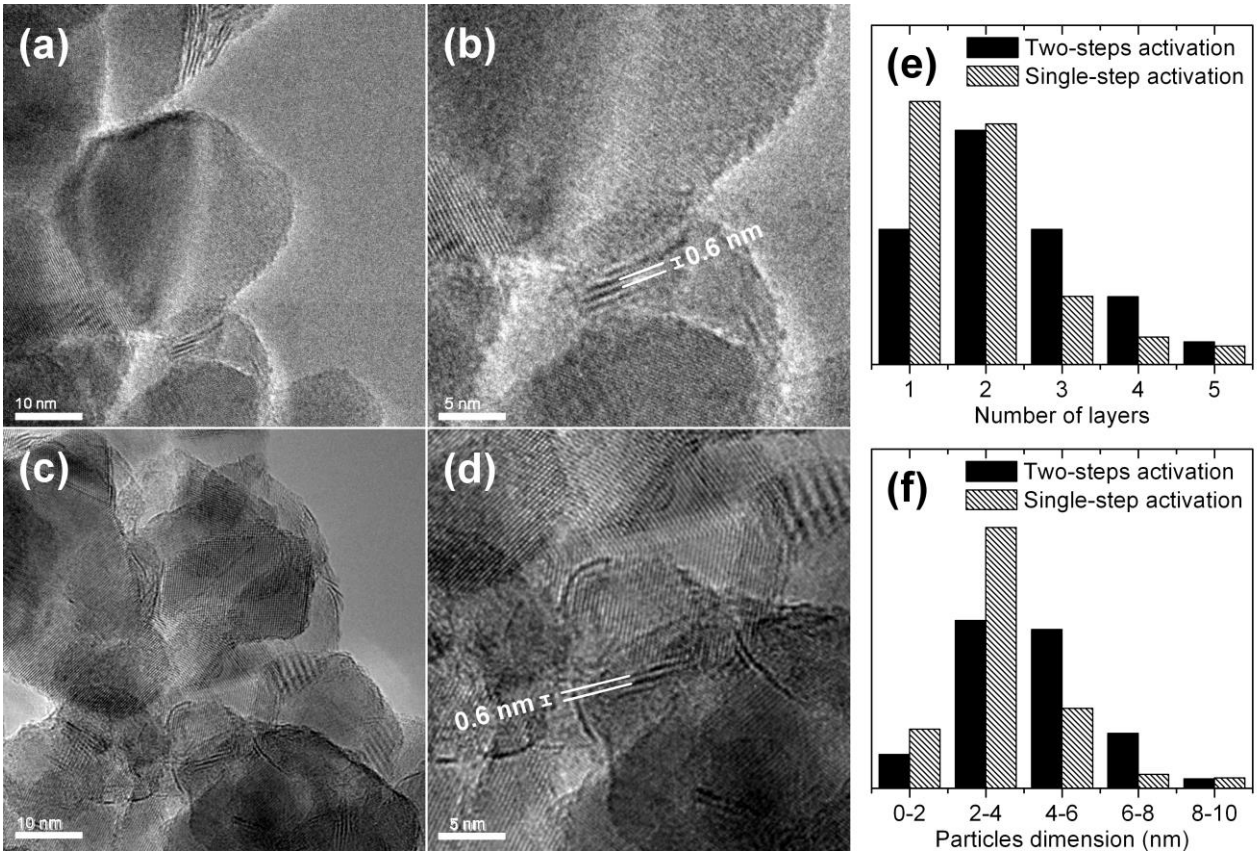

Figure 7. HRTEM images of the samples after the last sulfidation step: of the two-steps activation (**a, b**) and the single-step activation (**c, d**). The histograms show the average stacking of the MoS_2 particles along the *c* axis (**e**) and the MoS_2 particles length distribution (**f**).

3.5. Catalytic tests

Catalysts activities were determined as a pseudo first order rate constant, *k* which is calculated on the basis of the 8 measured conversions of: (i) DBT for HDS reaction; (ii) IND for HDN reaction; and (iii) NAP for HDY reaction. The rate constant *k* was calculated using the equation for the first order rate law and the correlation between residence time *t* and weight hourly space velocity (*WHSV*) is defined in the following equations:

$$\ln\left(\frac{[\mathrm{x}]}{[\mathrm{x}]_0}\right) = -\,\mathrm{kt} \Leftrightarrow \ln\left(\frac{[\mathrm{x}]_0 - conv.\cdot[\mathrm{x}]_0}{[\mathrm{x}]_0}\right) = -\,\mathrm{kt} \Leftrightarrow \ln(1-\mathrm{conv.}) = -\,\mathrm{kt}\,, \qquad (1)$$

where $[x]$ is the concentration of DBT/IND/NAP at time *t*, $[x]_0$ is the concentration of DBT/IND/NAP at time $t = 0$ and *conv.* is the fractional conversion of DBT/IND/NAP.
At steady state conditions the catalyst produces a product stream of steady composition. The time *t* in the first order kinetic equation is therefore the residence time of the feed in the reactor. This residence time is equal to the reciprocal *WHSV* defined as:

$$WHSV = \frac{flow \times\ feed\ \ density}{catalyst\ \ mass} \qquad (2)$$

, and thus get:

$$k = -WHSV \cdot ln(1 - conv.) \qquad (3)$$

Table 3. Summary of the catalytic tests on one- and two-steps activation samples in the hydrodesulfurization (HDS) of dibenzothiophene (DBT), hydrodenitrogenation (HDN) of indole (IND) and hydrogenation (HYD) of naphthalene (NAP) reactions.

	k(HDS)/h^{-1}	k(HDN)/h^{-1}	k(HYD)/h^{-1}
One-step activation	0.9	19.7	5.2
Two-steps activation	0.6	14.7	3.8

The results of the catalytic testing are summarized in Table 3. The one-step activation clearly leads to a better performance in all three reactions. For the rate of desulfurization the difference is most prominent as the one-step activation results in a 33% higher pseudo rate constant. These results agreed with the whole characterization work that showed how the one-step activation results in smaller MoS_2 nanoparticles in terms of both average diameter of the plates and number of stacking layers, i.e. expected to expose a larger number of active sites.

4. Conclusions

The present work highlights the importance of the activation procedure of HDS catalysts to determine the final structure and morphology of the MoS_2 active phase. A low loading Mo/TiO_2 catalyst has been chosen as an optimal model system to be analysed by a combination of spectroscopy, microscopy and diffraction techniques. The different complementary techniques allowed the collection of high quality data, indispensable to acquire a complete picture of the system.

The combination of morphology and nanometer size of the MoS_2 particles, resulting in a defect-rich surface structure, are the probable cause of the significant deviation of the Raman spectra from what is reported in the literature. The results demonstrate the unreliability of the frequency-layering model proposed for the interpretation of Raman in the case of a bottom-up synthetic approach, typically applied in heterogeneous catalysis.

The growth mechanism of MoS_2 particles on the oxide support is substantially related to the sulfiding atmosphere, in particular depending on the presence/absence of hydrogen (Figure 8). For the two-steps activation, where H_2S and H_2 are introduced sequentially, a partial sulfidation of the MoO_x species occurs at low temperatures, while the formed Mo-oxysulfide phase further evolves into well formed MoS_2 as the temperature increases.

A direct transformation of MoO_x species to MoS_2 particles is observed in the single-step activation instead. The synergy of H_2S and H_2 allows for easier oxygen depletion and substitution by sulfur around the Mo centers. Even at very low treatment temperatures no significant amount of Mo-oxysulfides have been detected.

A fine tuning of the activation parameters has been exploited to produce nanosized MoS_2 clusters with controlled morphology. Catalytic tests indicate that the MoS_2 nanoparticles obtained via the one-step activation method (characterized by smaller size distributions in terms of both average diameter of the plates and number of stacking layers) result more active in HDS, HDN and HYD catalysis.

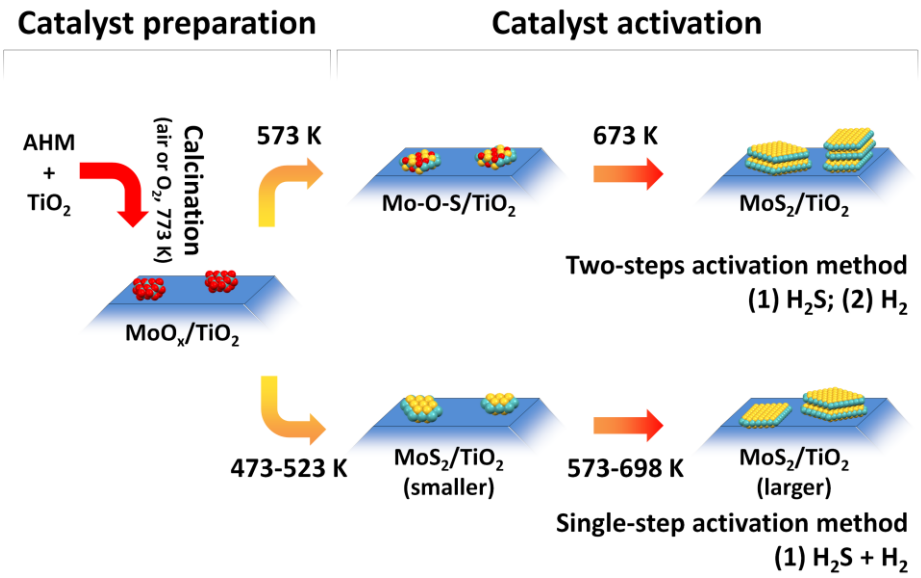

Figure 8. Schematic representation of the effect of the activation procedures on the supported MoS_2 structures.

Acknowledgements

The work has been financially supported by FIRB (RBAP115AYN). AB and CL acknowledge the Mega-grant of the Russian Federation Government to support scientific research under the at Southern Federal University, No. 14.Y26.31.0001.

References

[1] J. Heising, M.G. Kanatzidis, J. Am. Chem. Soc., 121 (1999) 11720.
[2] R.F. Sebenik, A.R. Burkin, R.R. Dorfler, J.M. Laferty, G. Leichtfried, H. Meyer-Grünow, P.C.H. Mitchell, M.S. Vukasovich, D.A. Church, G.G. Van Riper, J.C. Gilliland, S.A. Thielke, Molybdenum and Molybdenum Compounds, in: Ullmann's Encyclopedia of Industrial Chemistry, Wiley-VCH Verlag GmbH & Co. KGaA, 2000.
[3] B. Radisavljevic, A. Radenovic, J. Brivio, V. Giacometti, A. Kis, Nature Nanotech., 6 (2011) 147.
[4] Z. Yin, H. Li, H. Li, L. Jiang, Y. Shi, Y. Sun, G. Lu, Q. Zhang, X. Chen, H. Zhang, ACS Nano, 6 (2012) 74.
[5] B.C. Windom, W.G. Sawyer, D.W. Hahn, Tribol. Lett., 42 (2011) 301.
[6] X. Zong, H. Yan, G. Wu, G. Ma, F. Wen, L. Wang, C. Li, J. Am. Chem. Soc., 130 (2008) 7176.
[7] Q. Xiang, J. Yu, M. Jaroniec, J. Am. Chem. Soc., 134 (2012) 6575.
[8] H.C. Topsøe, B.; Massoth, F., Hydrotreating Catalysis and Science and Technology, Springer-Verlag, Berlin/Heidelberg, 1996.
[9] C.J.H. Jacobsen, E. Tornqvist, H. Topsoe, Catal. Lett., 63 (1999) 179.
[10] K.G. Knudsen, B.H. Cooper, H. Topsoe, Appl. Catal. A: Gen., 189 (1999) 205.
[11] N. Panariti, A. Del Bianco, G. Del Piero, M. Marchionna, Appl. Catal. A: Gen., 204 (2000) 203.
[12] European Parliament and Council, Directive 2009/30/EC, 150 (2009) 88.
[13] US Environmental Protection Agency, Control of Air Pollution From Motor Vehicles: Tier 3 Motor Vehicle Emission and Fuel Standards 79 (2014) 23414.
[14] H. Topsoe, B. Hinnemann, J.K. Norskov, J.V. Lauritsen, F. Besenbacher, P.L. Hansen, G. Hytoft, R.G. Egeberg, K.G. Knudsen, Catal. Today, 107-08 (2005) 12.
[15] H. Topsoe, Appl. Catal. A: Gen., 322 (2007) 3.
[16] M. Daage, R.R. Chianelli, J. Catal., 149 (1994) 414.
[17] K.S. Novoselov, D. Jiang, F. Schedin, T.J. Booth, V.V. Khotkevich, S.V. Morozov, A.K. Geim, Proce. Nat. Ac. Sci. USA, 102 (2005) 10451.

[18] H. Li, Q. Zhang, C.C.R. Yap, B.K. Tay, T.H.T. Edwin, A. Olivier, D. Baillargeat, Adv. Funct. Mater., 22 (2012) 1385.
[19] J.N. Coleman, M. Lotya, A. O'Neill, S.D. Bergin, P.J. King, U. Khan, K. Young, A. Gaucher, S. De, R.J. Smith, I.V. Shvets, S.K. Arora, G. Stanton, H.Y. Kim, K. Lee, G.T. Kim, G.S. Duesberg, T. Hallam, J.J. Boland, J.J. Wang, J.F. Donegan, J.C. Grunlan, G. Moriarty, A. Shmeliov, R.J. Nicholls, J.M. Perkins, E.M. Grieveson, K. Theuwissen, D.W. McComb, P.D. Nellist, V. Nicolosi, Science, 331 (2011) 568.
[20] H. Matte, A. Gomathi, A.K. Manna, D.J. Late, R. Datta, S.K. Pati, C.N.R. Rao, Angew. Chem.-Int. Edit., 49 (2010) 4059.
[21] L.P. Hansen, Q.M. Ramasse, C. Kisielowski, M. Brorson, E. Johnson, H. Topsoe, S. Helveg, Angew. Chem.-Int. Edit., 50 (2011) 10153.
[22] F. Cesano, S. Bertarione, A. Piovano, G. Agostini, M.M. Rahman, E. Groppo, F. Bonino, D. Scarano, C. Lamberti, S. Bordiga, L. Montanari, L. Bonoldi, R. Millini, A. Zecchina, Catal. Sci. Technol., 1 (2011) 123.
[23] R.I. Walton, A.J. Dent, S.J. Hibble, Chem. Mater., 10 (1998) 3737.
[24] S. Texier, G. Berhault, G. Perot, V. Harle, F. Diehl, J. Catal., 223 (2004) 404.
[25] S. Bouwens, F.B.M. Vanzon, M.P. Vandijk, A.M. Vanderkraan, V.H.J. Debeer, J.A.R. Vanveen, D.C. Koningsberger, J. Catal., 146 (1994) 375.
[26] O.Y. Gutierrez, T. Klimova, J. Catal., 281 (2011) 50.
[27] G. Bellussi, G. Rispoli, D. Molinari, A. Landoni, P. Pollesel, N. Panariti, R. Millini, E. Montanari, Catal. Sci. Technol., 3 (2013) 176.
[28] L.P.A.F. Elst, S. Eijsbouts, A.D. van Langeveld, J.A. Moulijn, J. Catal., 196 (2000) 95.
[29] L.S. Byskov, J.K. Norskov, B.S. Clausen, H. Topsoe, J. Catal., 187 (1999) 109.
[30] P. Raybaud, Appl. Catal. A: Gen., 322 (2007) 76.
[31] P.G. Moses, L.C. Grabow, E.M. Fernandez, B. Hinnemann, H. Topsoe, K.G. Knudsen, J.K. Norskov, Catal. Lett., 144 (2014) 1425.
[32] J.V. Lauritsen, M.V. Bollinger, E. Laegsgaard, K.W. Jacobsen, J.K. Norskov, B.S. Clausen, H. Topsoe, F. Besenbacher, J. Catal., 221 (2004) 510.
[33] J.V. Lauritsen, J. Kibsgaard, S. Helveg, H. Topsoe, B.S. Clausen, E. Laegsgaard, F. Besenbacher, Nature Nanotech., 2 (2007) 53.
[34] H. Topsoe, B.S. Clausen, Appl. Catal., 25 (1986) 273.
[35] H. Topsoe, B.S. Clausen, N.Y. Topsoe, E. Pedersen, Ind. Eng. Chem. Fund., 25 (1986) 25.
[36] J.K. Norskov, B.S. Clausen, H. Topsoe, Catal. Lett., 13 (1992) 1.
[37] N.Y. Topsoe, H. Topsoe, J. Catal., 139 (1993) 641.
[38] A. Stanislaus, B.H. Cooper, Catal. Rev.-Sci. Eng., 36 (1994) 75.
[39] B.C. Gates, H. Topsoe, Polyhedron, 16 (1997) 3213.
[40] S. Helveg, J.V. Lauritsen, E. Laegsgaard, I. Stensgaard, J.K. Norskov, B.S. Clausen, H. Topsoe, F. Besenbacher, Phys. Rev. Lett., 84 (2000) 951.
[41] J.V. Lauritsen, S. Helveg, E. Laegsgaard, I. Stensgaard, B.S. Clausen, H. Topsoe, E. Besenbacher, J. Catal., 197 (2001) 1.
[42] H. Topsoe, J. Catal., 216 (2003) 155.
[43] J.V. Lauritsen, M. Nyberg, J.K. Norskov, B.S. Clausen, H. Topsoe, E. Laegsgaard, F. Besenbacher, J. Catal., 224 (2004) 94.
[44] J.V. Lauritsen, J. Kibsgaard, G.H. Olesen, P.G. Moses, B. Hinnemann, S. Helveg, J.K. Norskov, B.S. Clausen, H. Topsoe, E. Laegsgaard, F. Besenbacher, J. Catal., 249 (2007) 220.
[45] P.G. Moses, B. Hinnemann, H. Topsoe, J.K. Norskov, J. Catal., 248 (2007) 188.
[46] A. Tuxen, J. Kibsgaard, H. Gobel, E. Laegsgaard, H. Topsoe, J.V. Lauritsen, F. Besenbacher, ACS Nano, 4 (2010) 4677.
[47] Y.Y. Zhu, Q.M. Ramasse, M. Brorson, P.G. Moses, L.P. Hansen, C.F. Kisielowski, S. Helveg, Angew. Chem.-Int. Edit., 53 (2014) 10723.
[48] P. Beato, E. Schachtl, K. Barbera, F. Bonino, S. Bordiga, Catal. Today, 205 (2013) 128.
[49] B.S. Clausen, H. Topsoe, Catal. Today, 9 (1991) 189.
[50] S. Najmaei, Z. Liu, P.M. Ajayan, J. Lou, Appl. Phys. Lett., 100 (2012) 6501.
[51] S. Najmaei, P.M. Ajayan, J. Lou, Nanoscale, 5 (2013) 9758.
[52] J.D. Grunwaldt, S. Hannemann, J. Goettlicher, S. Mangold, M.A. Denecke, A. Baiker, Phys. Scr., T115 (2005) 769.
[53] B. Ravel, M. Newville, J. Synchrotron Rad., 12 (2005) 537.
[54] A.L. Ankudinov, B. Ravel, J.J. Rehr, S.D. Conradson, Phys. Rev. B, 58 (1998) 7565.
[55] E. Groppo, C. Prestipino, C. Lamberti, P. Luches, C. Giovanardi, F. Boscherini, J. Phys. Chem. B, 107 (2003) 4597.
[56] E. Borfecchia, S. Maurelli, D. Gianolio, E. Groppo, M. Chiesa, F. Bonino, C. Lamberti, J. Phys. Chem. C, 116 (2012) 19839.
[57] L.W. Zhang, H.B. Fu, Y.F. Zhu, Adv. Funct. Mater., 18 (2008) 2180.
[58] G. Mestl, T.K.K. Srinivasan, Cat. Rev. - Sci. Eng., 40 (1998) 451.
[59] G.L. Schrader, C.P. Cheng, J. Catal., 80 (1983) 369.

[60] E.K. Payen, S.; Houssenbay, S.; Szymanski, R.; Grimbolt, J., J. Phys. Chem., 93 (1989) 6501.
[61] C. Lee, H. Yan, L.E. Brus, T.F. Heinz, J. Hone, S. Ryu, ACS Nano, 4 (2010) 2695.
[62] B. Chakraborty, H.S.S.R. Matte, A.K. Sood, C.N.R. Rao, J. Raman Spectrosc., 44 (2013) 92.
[63] G. Mestl, N.F.D. Verbruggen, H. Knozinger, Langmuir, 11 (1995) 3035.
[64] M. Dieterle, G. Weinberg, G. Mestl, Phys. Chem. Chem. Phys., 4 (2002) 812.
[65] A. Splendiani, L. Sun, Y. Zhang, T. Li, J. Kim, C.-Y. Chim, G. Galli, F. Wang, Nano Lett., 10 (2010) 1271.
[66] H. Shi, R. Yan, S. Bertolazzi, J. Brivio, B. Gao, A. Kis, D. Jena, H.G. Xing, L. Huang, ACS Nano, 7 (2013) 1072.
[67] A. Zecchina, D. Scarano, S. Bordiga, G. Spoto, C. Lamberti, Adv. Catal., 46 (2001) 265.
[68] C. Lamberti, E. Groppo, G. Spoto, S. Bordiga, A. Zecchina, Adv. Catal., 51 (2007) 1.
[69] C. Lamberti, A. Zecchina, E. Groppo, S. Bordiga, Chem. Soc. Rev., 39 (2010) 4951.
[70] S. Bordiga, E.E. Platero, C.O. Arean, C. Lamberti, A. Zecchina, J. Catal., 137 (1992) 179.
[71] S. Bordiga, D. Scarano, G. Spoto, A. Zecchina, C. Lamberti, C.O. Arean, Vib. Spectrosc., 5 (1993) 69.
[72] L. Mino, A.M. Ferrari, V. Lacivita, G. Spoto, S. Bordiga, A. Zecchina, J. Phys. Chem. C, 115 (2011) 7694.
[73] E. Guglielminotti, E. Giamello, J. Chem. Soc., Faraday Trans. 1, 81 (1985) 2307.
[74] V. Bolis, A. Barbaglia, S. Bordiga, C. Lamberti, A. Zecchina, J. Phys. Chem. B, 108 (2004) 9970.
[75] F. Mauge, J. Lamotte, N.S. Nesterenko, O. Manoilova, A.A. Tsyganenko, Catal. Today, 70 (2001) 271.
[76] S. Bordiga, E. Groppo, G. Agostini, J.A. van Bokhoven, C. Lamberti, Chem. Rev., 113 (2013) 1736.
[77] L. Mino, G. Agostini, E. Borfecchia, D. Gianolio, A. Piovano, E. Gallo, C. Lamberti, J. Phys. D: Appl. Phys., 46 (2013) 3001.